

Angular Resolved RCS and Doppler Analysis of Human Body Parts in Motion

Sevda Abadpour¹, Member, IEEE, Mario Pauli², Senior Member, IEEE, Christian Schyr, Florian Klein, Rene Degen³, Jan Siska⁴, Member, IEEE, Nils Pohl⁵, Senior Member, IEEE, and Thomas Zwick⁶, Fellow, IEEE

Abstract—The backscattering models of complex traffic targets play a critical role in the current evolution of over-the-air (OTA) validation test methods and, consequently, the validation and verification of advanced driver assistance systems (ADAS). Furthermore, stimulating the operational behavior of the automotive radar sensor in an OTA vehicle-in-the-loop (ViL) environment requires radar cross section (RCS) and Doppler signatures related to the movement of vulnerable road users (VRUs), especially pedestrians in traffic scenarios. These RCS and Doppler signatures of human motion can be retrieved by evaluating the range-Doppler behavior of the motions from the human extremities. High-resolution RCS measurements in the radial and angular domains can be applied to micro-Doppler models of human motions and significantly improve them. Therefore, this work presents a measurement technique to estimate the radar reflectivity of different scattering points of human body regions in different moving scenarios. The necessary signal processing steps are discussed in detail for assigning the corresponding RCS values and Doppler signature to the time-varying scattering points from the different extremities of a human body. The measurement results can be used to develop more realistic models of a person in motion in a real traffic scenario which is worthwhile in radar channel wave propagation, target recognition, and classification.

Index Terms—Displacement measurement, Doppler measurement, human body radar cross section (RCS) measurement, human body regions, human motion, motion capture (MoCap) data, radar high-resolution measurement, range-Doppler, RCS-modeling of extended targets, scattering points.

Manuscript received 9 August 2022; revised 12 October 2022; accepted 21 October 2022. This work was supported by the German Federal Ministry of Education and Research (BMBF) through the Virtuelle Validierung (CADJapanGermany) (VIVID) Project under Grant 16ME0171. (Corresponding author: Sevda Abadpour.)

This work involved human subjects or animals in its research. Approval of all ethical and experimental procedures and protocols was granted by the Ethics Committee of Karlsruhe Institute of Technology (KIT).

Sevda Abadpour, Mario Pauli, and Thomas Zwick are with the Institute of Radio Frequency Engineering and Electronics (IHE), Karlsruhe Institute of Technology (KIT), 76131 Karlsruhe, Germany (e-mail: sevda.abadpour@kit.edu).

Christian Schyr is with AVL Deutschland GmbH, 76229 Karlsruhe, Germany.

Florian Klein is with HHVISION, 50827 Cologne, Germany.

Rene Degen is with the Faculty of Automotive Systems and Production, Cologne University of Applied Sciences, 50679 Cologne, Germany.

Jan Siska and Nils Pohl are with the Institute for Integrated Systems, Ruhr University Bochum, 44801 Bochum, Germany.

Color versions of one or more figures in this article are available at <https://doi.org/10.1109/TMTT.2022.3218304>.

Digital Object Identifier 10.1109/TMTT.2022.3218304

I. INTRODUCTION

THE observation of vulnerable road users (VRUs) motion, especially pedestrians and bicyclists, with mm-Wave radar systems is widely used to simulate their motion in the field of autonomous driving (AD). Human motions give rise to Doppler modulations in radar signatures [1] which can be employed for modeling human activities. These micro-Doppler signals can be used for the target recognition, classification, and preparing a realistic backscattering model of human activities [2], [3], [4], [5], [6]. Developing precise radar target models is an essential prerequisite to simulating a highly realistic wave propagation that is as close as possible to a real environment. Only in this case the qualification and functionality of automotive radars can be examined extensively, even in complex traffic situations [7].

The detailed model of VRUs can be represented by modeling the backscattering behavior of the traffic participants in the radial and angular domains in combination with the micro-Doppler signature [2]. The human micro-Doppler signatures are already reported in the literature based on the electromagnetic (EM) simulation and measurements [8], [9], [10], [11], [12], [13]. The drawback of modeling based on numerical methods is its excessive computational requirements, especially when modeling the time-varying geometries is of interest [1].

A precise radar model of human motions requires the knowledge of the backscattering behavior of human body regions in combination with their dynamic description. The backscattering behavior can be determined by high-resolution radar cross section (RCS) measurements [2] which are based on the scattering points modeling of extended radar targets. Realistic human motion data can be gathered by optical motion capture (MoCap) facilities [8]. In [14], the human is modeled as a multipoint scatterer, where the scattering coefficient of each point is calculated by a raytracing algorithm, and the position of points caused by human movement is collected from computer animation data. However, the predicted backscattering coefficient of the points does not include the multipath interactions between the different parts of the human regions and shadowing that decreases the accuracy of the method. One solution which allows for the development of a highly accurate and realistic model is determining the RCS values of the scattering points based on high-resolution RCS measurements in range and as well in an angular direction.

Therefore in this work, a measurement technique is proposed from the combination of high-resolution RCS measurement and MoCap technology [15] to accurately estimate the radar reflectivity of each scattering point on human body regions and extract their radar signatures, e.g., range-time, Doppler-time, and range-Doppler. Subsequently, that makes it possible to generate an accurate, high-resolution, and realistic backscattering model of human extremities. The extracted radar models can be employed in the target recognition, classification, and data training for machine learning methods, e.g., generative adversarial networks (GANs) [16], [17], [18].

In this context, the article is organized as follows. Section II discusses the fundamentals for accurate radar signature extraction from the measured radar data and collecting human motion data. The extension of the classical frequency evaluation (FE) is discussed in detail in Section II-A. It is employed to analyze the measurement data based on a frequency-modulated continuous-wave (FMCW) radar sensor. The fast-time measurement¹ data can be examined by the discussed enhanced frequency evaluation (EFE) algorithm for highly accurate range and either Doppler frequency analysis or velocity analysis. Section III describes the utilized high-resolution RCS measurement setup in combination with the MoCap technique for collecting the radar raw data of human activities and the postprocessing. The accuracy of the EFE technique is verified by the reference measurement in Section III-A. Accordingly, dedicated measurements are arranged to scan a volunteer person with the different motions. The person is dressed up with MoCap cloth, and MoCap trackers are attached to different body regions. Section IV demonstrates the extraction of the range-velocity radar signature of human motion, which is used for modeling the backscattering behavior of human activities. This section also describes the proposed signal processing chain and the required calibration measurement for preparing authentic radar models. Finally, Section V concludes this work.

II. THEORY

A high-resolution monostatic RCS measurement setup is utilized for the RCS determination of different body regions of a human in motion. The radar signature extraction method from the collected radar raw data is presented in Section II-A. This section introduces the signal processing chain to extract the range and Doppler signatures of the collected measurement radar data with a linear FMCW radar. Intermediate frequency (IF) is evaluated based on the fast-time measurement data, which has a considerably higher measurement rate in comparison with the ramp repetition rate. That enables the technique to resolve the spatially sensing of multiple simultaneously moving scattering points of an extended object under test. The utilized MoCap technology for collecting the human motion data is explained in Section II-B.

A. Range and Doppler Determination Using High-Resolution mm-Wave Radar Sensor

Different human movements produce distinctive micro-Doppler signatures in different human body regions. This

type of motion, in the presence of the radar illumination, creates distinguishable micro-Doppler signatures of each body part which helps to identify and model human activities and produce specific radar targets in different motion activities. Therefore, the measured range to the different human body regions, $R_m(t)$, is not constant but swings around R (distance between the radar sensor and the center of the object under test at stationary) with an amplitude of $A_{m'}$ and frequency of $f_{m'}$

$$R_m(t) = R + \sum_{m'} A_{m'} \cos(2\pi f_{m'} t). \quad (1)$$

It is assumed that the targets are moving radially to the Radar system.

Highly accurate and robust distance measurement with an FMCW radar is discussed in [19], [20], [21], [22], and [23]. The intermediate FE can be utilized to analyze the collected IF signal from the radar measurement. The IF signal of a monostatic FMCW radar is the downconverted version of the received signal by the radar. It can be written as

$$s_{if}(t) = A_{if} \cos\left(\alpha\tau t \pm 2\pi f_0\tau - \frac{1}{2}\alpha\tau^2\right), \quad 0 \leq t \leq T_{\text{sweep}} \quad (2)$$

where A_{if} is the amplitude of IF signal, f_0 is the sweep center frequency of FMCW radar, α is the ramp slope which is the quotient of the ramp bandwidth (Δf) and the ramp time (T_{sweep}), τ is the round trip propagation delay of a target which is located in the range of $R_m(t)$, and sign \pm applies to up ramp and down ramp, respectively. Fig. 1(a) illustrates time–frequency domain representation of the transmitted and received frequencies for a triangular waveform of an FMCW radar and its specifications. In this work, the classical FE technique is denoted as the basic frequency evaluation (BFE) technique which is applicable to the sawtooth shape modulation. An FMCW radar transmits M consecutive ramps; therefore, the idealized IF signal can be described as a two-dimensional (2-D) signal which is the function of time (t) and ramp index number (j)

$$s_{if}(t, j) = s_{if}(t + (j - 1)T_{\text{sweep}}), \quad j \in \mathbb{Z}, \quad 1 \leq j \leq M. \quad (3)$$

This IF signal $s_{if}(t, j)$ is sampled with the sampling rate of the radar ADC (f_s) for each individual ramp signal. This results in N samples for each ramp within the time duration of T_{sweep}

$$N = f_s \cdot T_{\text{sweep}}. \quad (4)$$

The resulting samples are stored in a 2-D matrix of the size $N \times M$. The sampled IF signal of every individual ramp is saved column-wise with a fast-time index of n , and the collected data of the M ramps are stored in the rows of the matrix with a slow-time² index of j , as shown in Fig. 1(b). Therefore, the stored IF data of the FMCW radar can be described as a function of fast- and slow-time indexes, $S_{if}(n, j)$.

¹Corresponding to the sampled IF data with the sampling rate of the radar ADC (f_s) to collect samples within the time duration of each ramp.

²Measurement with ramp duration time ($1/T_{\text{sweep}}$).

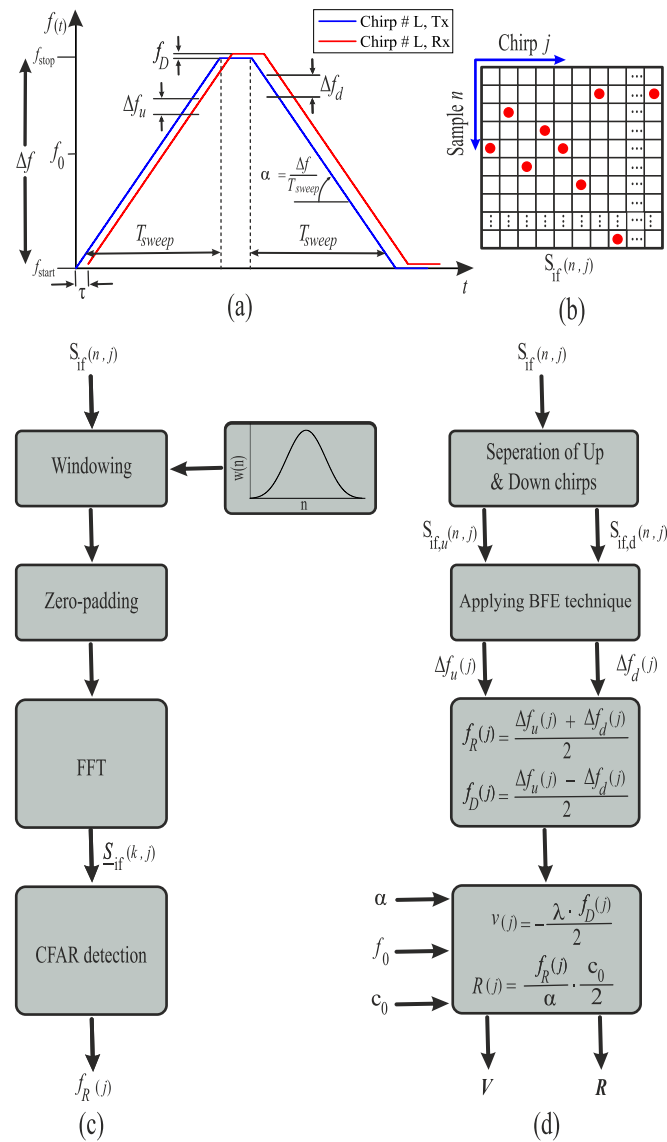


Fig. 1. (a) Transmitted (blue) and received (red) frequencies of a triangular waveform for the FMCW radar system. The chirp consists of two ramps of opposite slopes, both with a duration of T_{sweep} . Note that the chirp (L, Rx) is drawn with a small positive Doppler shift of f_D . (b) Illustration of the stored IF data structure in the direction of slow- and fast-time axis from the measurement using an FMCW radar system. (c) Signal processing chain for determining the related IF in the location of the object under test by the BFE technique. (d) Signal processing chain of the EFE technique for estimating the range and velocity of the radar target from the collected radar raw data. A combination of two frequency chirps is processed individually by BFE.

The range information can be calculated by analyzing the frequency information of the IF signal on the fast-time axis. Fig. 1(c) shows the signal processing chain of the BFE technique, which determines the corresponding IF [$f_R(j)$] for calculating the range of the targets to the Radar system. Equation (5) shows a typical relationship for determining the distance from the radar target to the Radar system

$$R(\tau) = \frac{c_0}{2} \cdot \tau = \frac{c_0}{2} \cdot \frac{f_{if}(\tau)}{\alpha} \quad (5)$$

where c_0 is the propagation speed of the EM wave in the air. The signal processing chain in Fig. 1(c) starts with preprocessing the stored IF data by windowing. Then, zero-padding is

applied to increase the frequency display resolution. The fast Fourier transform (FFT) processes $S_{if}(n, j)$ to determine the spectrum of the FFT, $\underline{S}_{if}(k, j)$, where k is the IF index. The radar targets are detected in range by applying the CFAR algorithm on the magnitude of $\underline{S}_{if}(k, j)$ and subsequently determining the IF corresponding to the distance to the radar target.

The radial velocity of the radar targets cannot be estimated directly from the traditional sawtooth waveform since the Doppler frequency cannot be distinguished from the IF. For this reason, a triangular shape is used in which the second ramp section has an opposite slope and the same ramp duration [24]. The range and velocity of the radar targets can be calculated by not-shifted IF and Doppler shift estimation during two adjacent up and down ramps in the stored IF data matrix. The BFE algorithm can be enhanced by this technique, and the signal processing chain of the EFE algorithm is shown in Fig. 1(d). The input of the algorithm is the sampled IF data [$S_{if}(n, j)$] which is collected from the measurement by triangular-shaped frequency chirps. Then the algorithm produces two matrices in which the IF data of up ramps [$S_{if,u}(n, j)$] and down ramps [$S_{if,d}(n, j)$] are stored separately. Subsequently, the algorithm applies the BFE algorithm on $S_{if,u}(n, j)$ and $S_{if,d}(n, j)$ to calculate $\Delta f_u(j)$ and $\Delta f_d(j)$ from the difference between the IF data of two successive ramps with the same slope [see Fig. 1(a)]. The range related IF [$f_R(j)$] and Doppler shift [$f_D(j)$] in the fast-time measurement data can be calculated by

$$\begin{aligned} f_R(j) &= \frac{\Delta f_u(j) + \Delta f_d(j)}{2} \\ f_D(j) &= \frac{\Delta f_u(j) - \Delta f_d(j)}{2}. \end{aligned} \quad (6)$$

Subsequently, the algorithm estimates the range and the velocity of the radar targets in each chirp by

$$\begin{aligned} R(j) &= \frac{f_R(j)}{\alpha} \cdot \frac{c_0}{2} \\ v(j) &= -\frac{\lambda \cdot f_D(j)}{2}. \end{aligned} \quad (7)$$

Consequently, the algorithm presents the range matrix (\mathbf{R}) and the velocity matrix (\mathbf{V}) based on the fast-time index. This procedure allows to get RCS values with high resolution in range and also the velocity of the target. Furthermore, the additional rotation feature of the focused antenna of the Radar system (see Table I) makes it possible to have a high resolution in the azimuth and elevation. Thus, highly resolved range-velocity information of each part of a moving body is achievable.

B. Capturing Human Motion

Human motion data is collected by the MoCap technique [25] which employs NaturalPoint's OptiTrack tracking systems. This system is categorized as an outside-in system where MoCap sensors are outside and data sources inside the capture volume [26]. NaturalPoint's OptiTrack tracking system is an optical MoCap system that provides tracking data with the aid of Prime^X13 cameras and retro-reflective markers as

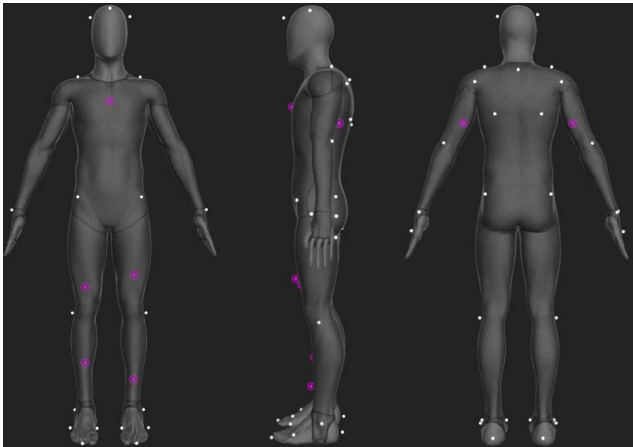


Fig. 2. Markers setup. White dots show the attached markers, which are used to create body joints and are placed around them. The purple markers can be seen as additional markers for the segments between the joints, i.e., the bones.

the MoCap markers. The cameras have a native resolution of 1280×1024 pixels and record with a native frame rate of 240 Hz, which corresponds to a latency of 4.2 ms. Cameras track the markers up to a depth of 16 m with a 3-D accuracy of ± 0.2 mm. These markers are illuminated by infrared LEDs with a light wavelength of 850 nm and are recorded with an 850 nm bandpass filter by the cameras. The focal length is 5.5 mm [27]. These cameras can have an arbitrary position and orientation to cover the capture volume. The corresponding software Motive 2.3.0 is used for solving the OptiTrack system and matching multiple 2-D camera images to reconstruct the 3-D information.

For full body tracking, the retro-reflective markers must be placed at the defined positions on a person's body. This is shown in Fig. 2. The information about the marker positions is gathered by the calibration process of the MoCap system. It includes a calibration process of wand and angle. The wand calibration contains retro-reflective markers of a specific size with a well-known distance toward each other. Therefore, the markers are labeled and assigned to certain body parts.

III. MEASUREMENT SETUP

A. Verification of the Utilized EFE Algorithm

In order to verify the EFE technique for analyzing the measured data and extracting the range-velocity information of the radar target, a radar measurement is conducted with a moving standard target. Thereby, the Radar system is installed in front of a linear magnetic track with a trihedral corner reflector (TCR) mounted onto a moving carriage. Fig. 3 illustrates the measurement setup. Table I shows the technical specification and configuration of the Radar system. The previous work [2] discusses the Radar system and high-resolution measurement setup in more detail.

A TCR with the inner height (a) of 19.9 cm is placed on the carriage to move 1.5 m away from the Radar system. The center of the TCR is aligned the main beam of the Radar system. The linear magnetic track has a maximum displacement range of 2.8 m and a positioning repeatability

TABLE I
RADAR SYSTEM TECHNICAL SPECIFICATION AND CONFIGURATION

Parameter	Radar system Specification
Center Frequency (f_0)	78.5 GHz
Bandwidth (Δf)	5 GHz
Half-Power Beam Width (HPBW)	1.3° in Azimuth and Elevation direction
Ramp Time (T_{sweep})	4.1 ms (sawtooth)
Antenna Gain (G)	40.5 dBi
Transmit Power (P_{Tx})	-6 dBm
Noise Figure (NF)	20 dB
Ramp Slope (α)	± 1.25 MHz/ μ s
ADC Sampling Rate (f_s)	1 MS/s

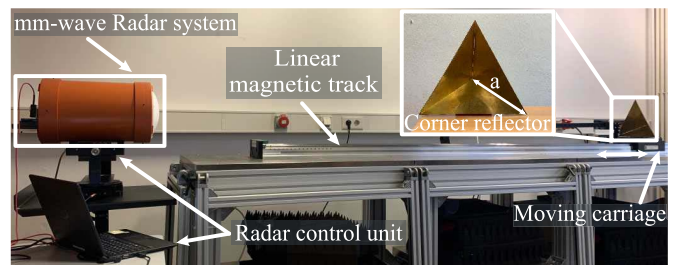


Fig. 3. Setup for validation of the EFE algorithm to extract the range-velocity information using a TCR, which can move on the linear magnetic track with controllable velocity and acceleration. The TCR is aligned to the main beam of the Radar system. The maximum displacement range in the setup is 2.8 m.

of $1 \mu\text{m}$. The carriage of the magnetic track has a maximum velocity and acceleration of 5 m/s and 30 m/s^2 , respectively. The carriage is accelerated to a velocity of $v = 2$ m/s. The number of ramps is set to 200, and the full ramp period to 5 ms. The full ramp period consists of the ramp duration time (T_{sweep}) and its dwell time. The maximum number of ramps and the ramp period is set to retrieve a measurement time that is long enough to evaluate the carriage motion with constant velocity and the subsequent deceleration process of 10 m/s^2 .

The measured radar data and extracted range-velocity information of the moving target are shown in Fig. 4. The range-velocity and velocity-time information of the moving process is shown in Fig. 4(a) and (b), respectively. That shows the TCR is positioned in the range of 2.52 m to the Radar system at the start of the movement process. Then, the radar target is stopped in the range of 3.77 m which corresponds to the chirp number of 67. Fig. 4(b) demonstrates that the radar target is displaced 1.5 m. The movement process has two steps, as can be seen in Fig. 4. The TCR is moved with a constant velocity of 2 m/s and a standard deviation of 0.023 m/s , initially. Then the deceleration starts with 9.9 m/s^2 in the last 0.36 m displacement. The experiment verifies that the algorithm is able to detect range and velocity information accurately.

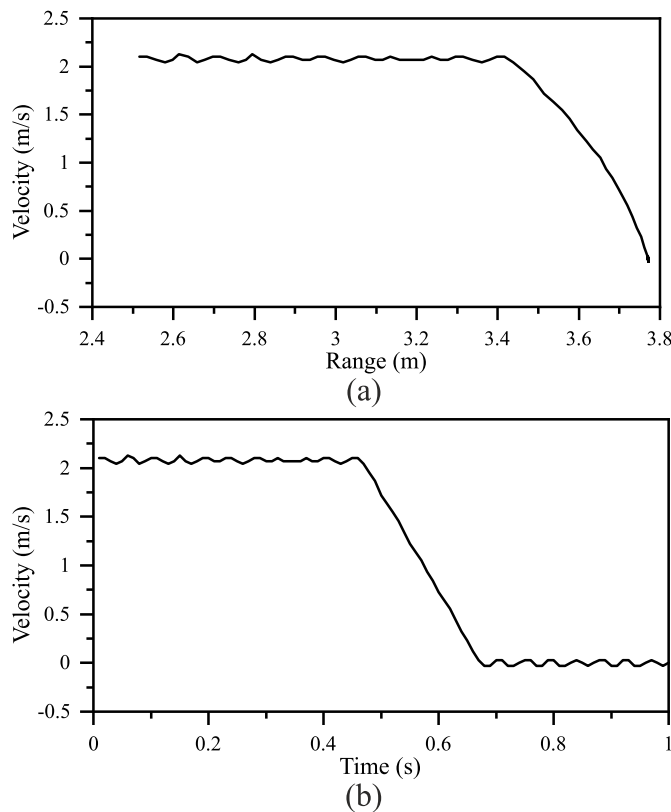


Fig. 4. Measured radar data of the moving TCR to validate the utilized EFE technique. The result of the algorithm is plotted as a range and velocity information of the radar target. The TCR is moved with a constant velocity of 2 m/s for 1.14 m and decelerated with 10 m/s for 0.36. (a) Velocity-range information of the moving TCR. (b) Calculated velocity of the TCR using the Doppler information from the EFE algorithm.

B. Setup for Extracting Velocity and RCS Information of a Human Body in Motion

With a dedicated setup, the range, velocity, and RCS information of individual body parts of a human in motion can be obtained. As shown in Section III-A, the presented EFE algorithm can be used to obtain the range and velocity information of a moving target from the collected radar raw data. As discussed in Section I and the previous work [2], assigning the Doppler signature with a verified RCS value to different extremities of a human body can be used to characterize the human activity and develop a realistic target model in wave propagation software. This section proposes a measurement setup for activity recognition and radar signature extraction by hybridizing the presented high-resolution monostatic RCS measurement setup and MoCap data of human motion. The Radar system and MoCap are controlled by MATLAB interface on a laptop and workstation, respectively. They communicate through a synchronization station and based on user datagram protocol (UDP). Upon receiving a radar initialization message from the Radar system, the synchronization station triggers the MoCap cameras to initiate data collection. Appropriate delays are incorporated in the MoCap and radar data collection to ensure that the MoCap data collection happens simultaneously with radar measurement data.

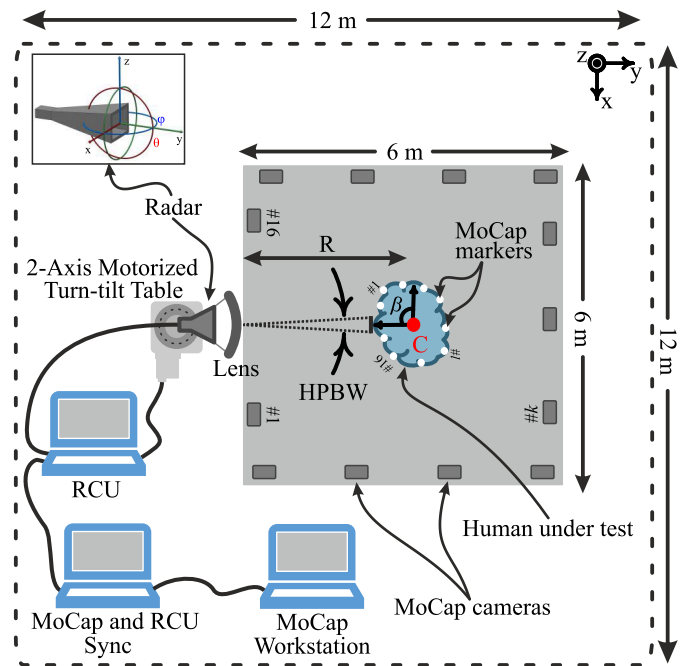


Fig. 5. Block diagram of measurement setup to detect the scattering points with their corresponding range, velocity, and RCS information of a human in motion for radar model extraction. The rotation angles of the radar in azimuth (ϕ) and elevation (θ) directions as well as the radar coordinate system are shown in the inset.

Fig. 5 shows the block diagram of the measurement setup. The presented measurement setup enables the collection of the MoCap data of human motion. Simultaneously, the radar raw data is collected for the high-resolution monostatic RCS measurement of the human extremities. A human is positioned at the range of R in the test setup for extracting the range, velocity, and verified RCS values from each region of the human body. The main beam of the Radar system is aligned to the center of the human under test. Therefore, half the height of the human corresponds to $\theta = 0^\circ$ which is the scanning angle of the Radar system in the elevation direction. The Radar system scanning angle in the azimuth direction, $\phi = 0^\circ$, is adjusted to the middle of the human shoulder width. Further details are discussed in Section IV.

For full body motion tracking, the retro-reflective markers are attached at defined positions on a volunteer person's body, as it is discussed in Section II-B. Sixteen Prime^X13 cameras are utilized in two planes differing in height to cover the capture volume as comprehensively as possible. That enables the MoCap system to measure the motion of each extremity by scanning with the Radar system. During human motion, the measurement regions are subdivided into three main regions, i.e., torso-head, hand, and leg, as shown in the inset of Fig. 6. The right and left sides of the body regions are separately scanned during the measurement. The MoCap synchronization station communicates wirelessly with MoCap markers and cameras. Fig. 6 shows the details of the measurement setup in the motion Lab environment provided by HHVISION company. The human under test is placed on the treadmill with an adjustable speed at a distance of 3.5 m from the Radar system. Subsequently, the radar is used to collect the range,

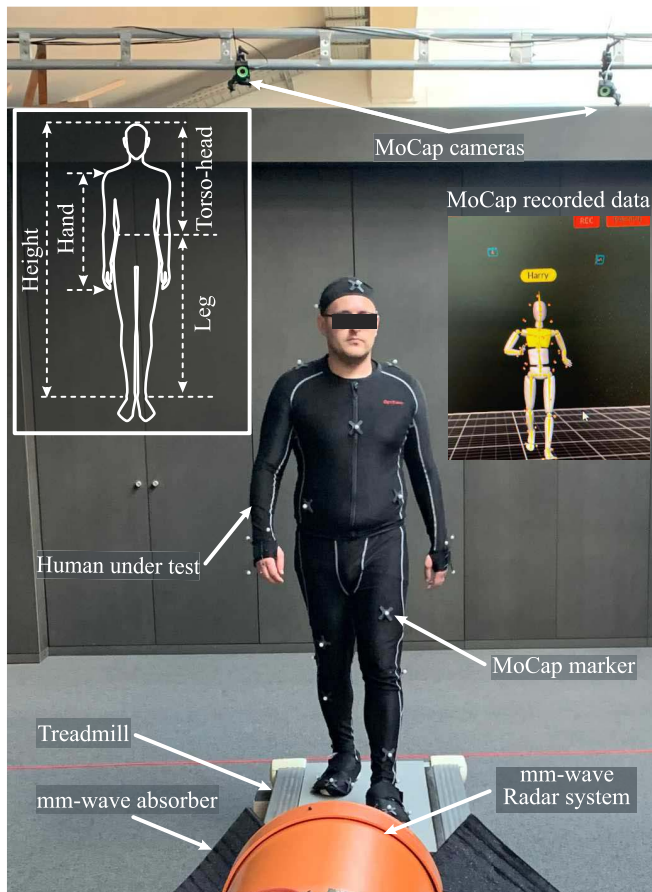


Fig. 6. Setup for extraction of range, velocity, and RCS information of different body parts of a human in motion. The defined corresponding body parts (torso-head, hand, and leg) for measurement of each body region are shown in the inset.

velocity, and RCS information of the body parts in motion. It should be noted that thin and flexible radar absorbers are used to prevent undesired reflections from the treadmill.

The effect of clothing has been thoroughly studied elsewhere [2], [28], [29], [30]. It is shown that, in the frequency range of 76–81 GHz, the clothing only has a minor effect on the RCS value in the range of 1–2 dB. Furthermore, it is concluded that wearing tight and thin clothing has little influence on the reflectivity behavior of the human body regions. In this work, the human under test is dressed up in a MoCap suit, which is very thin and tight. Therefore, the cloth is almost transparent and does not affect the RCS of the body itself significantly. However, this might change if special clothes are worn, e.g., with reflective elements.

The experiments are conducted to collect the radar raw data and the motion data of a human in walking and jogging situations. The scattering points, rang-velocity information, and verified RCS values of every body region are extracted in the postprocessing step, which is discussed in Section IV.

IV. MEASUREMENT RESULTS

This section describes the measurement results of a jogging and walking person. Fig. 7 shows the signal processing chain to extract the scattering points of the human in motion. To get

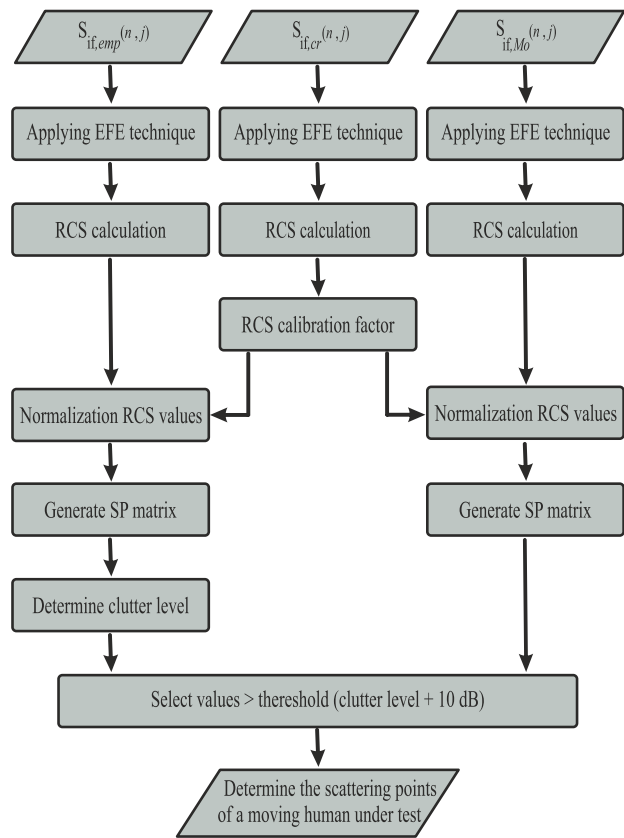


Fig. 7. Signal processing chain for extracting the scattering points of humans in motion from the high-resolution measurement data (SP matrix is the initial extracted scattering points matrix).

correct RCS values, a calibration procedure is necessary. This calibration process consists of two steps which are illustrated in Fig. 7. In the first step, the empty test environment $[S_{if,emp}(n, j)]$ is measured to determine the clutter level of the empty environment. $S_{if,emp}(n, j)$ is the stored IF data from the measurement environment in the absence of the test objects. In the second step, the amplitude of the measured values is normalized with respect to a known target, i.e., a standard corner reflector $[S_{if,cr}(n, j)]$ with a specific RCS value. $S_{if,cr}(n, j)$ is the collected radar data from the measurement of a TCR with an analytical RCS value of 0 dBsm. That is a calibration measurement to normalize the RCS values of the measurement for the object under test, as it is shown in Fig. 7. In order to obtain only reflections from the desired targets, either the human under test $[S_{if,Mo}(n, j)]$ or the calibration target, an additional gating in the spatial domain is used.

The combination of the discussed EFE technique in Section II-A and the subsequent calibration process enables the signal processing chain to determine the exact position of the scattering points on the surface of the human body with their corresponding RCS value and velocity.

To gather the data from the empty room, $S_{if,emp}(n, j)$, the test environment is scanned in the absence of the human under test with an angular resolution of 1° in both azimuth (φ) and elevation (θ) directions. The scanning area for calculating the clutter level of the test environment is set to $\pm 10^\circ$ in azimuth

and -19° to 17° in elevation directions. The maximum measured RCS value in every elevation angle is introduced as the clutter level in the related elevation plane. That prepares a clutter-level matrix based on the scanning elevation angle of the test environment and characterizes it in the absence of the test objects.

Finally, $S_{if,Mo}(n, j)$ contains the raw data of the radar measurement for a defined human motion and from the body region under study. The depicted signal processing chain in Fig. 7 introduces the object list (OL) of human motion with the following structure:

$$\mathbf{OL} = \begin{bmatrix} x''_1 & y''_1 & z''_1 & \text{RCS}_1 & f_{D1} & v_1 & t_1 \\ \vdots & \vdots & \vdots & \vdots & \vdots & \vdots & \vdots \\ x''_i & y''_i & z''_i & \text{RCS}_i & f_{Di} & v_i & t_i \\ \vdots & \vdots & \vdots & \vdots & \vdots & \vdots & \vdots \\ x''_P & y''_P & z''_P & \text{RCS}_P & f_{DP} & v_P & t_P \end{bmatrix} \quad (8)$$

where x''_i , y''_i , z''_i are the coordinates of the i th scattering point on the human extremities, RCS_i is its measured RCS value, f_{Di} , and v_i are its measured Doppler shift and velocity, t_i shows the instant of human motion related to the i th scattering point, and P is the total number of extracted points.

The measurements are performed for the test person in jogging and walking situations over the whole 360° azimuthal rotation angle with step widths of 90° . The Radar system in the test setup of Fig. 6 is scanning each body region of the human in motion with steps of $\Delta\varphi = 1^\circ$ and $\Delta\theta = 1^\circ$ in the azimuth and elevation direction, respectively. The scanning area is chosen in a way that, the complete body region of interest is covered. The number of chirps is configured to 256.

As proof of concept, the measured data and the body model with the measured points of the leg, head-torso, and hand are shown in Figs. 8–10, respectively. The person under test is jogging on the treadmill with a speed of 1.94 m/s. The Radar system scans the human under test from the front side ($\beta = 0^\circ$). Although each body region is measured and investigated with steps of 1° in azimuth and elevation directions, only range-velocity plots of a few elevations and azimuth scanning angles are shown in this article. The inset of each subfigure in Figs. 8–10 depicts the measured points in each body region, and the measured point in each subfigure is marked with red color.

Fig. 8(a)–(f) shows the different measurement points along the left leg of the jogging person. The range information is given on the x -axis of the plots, the y -axis of the plots represents the velocity information, and the RCS is coded in the color of the points. Fig. 8(a) shows that nearly all points are concentrated around the distance of 3.5 m with a velocity close to 0 m/s. This can easily be explained by the position of the measurement point of $\theta = 0^\circ$. These points belong to the waist of the body, and hence it shows only slight movement during the motion. With increasing distance from the torso, i.e., along the leg, the movement of the measured points increases. This results in a higher velocity of the measured point and also in

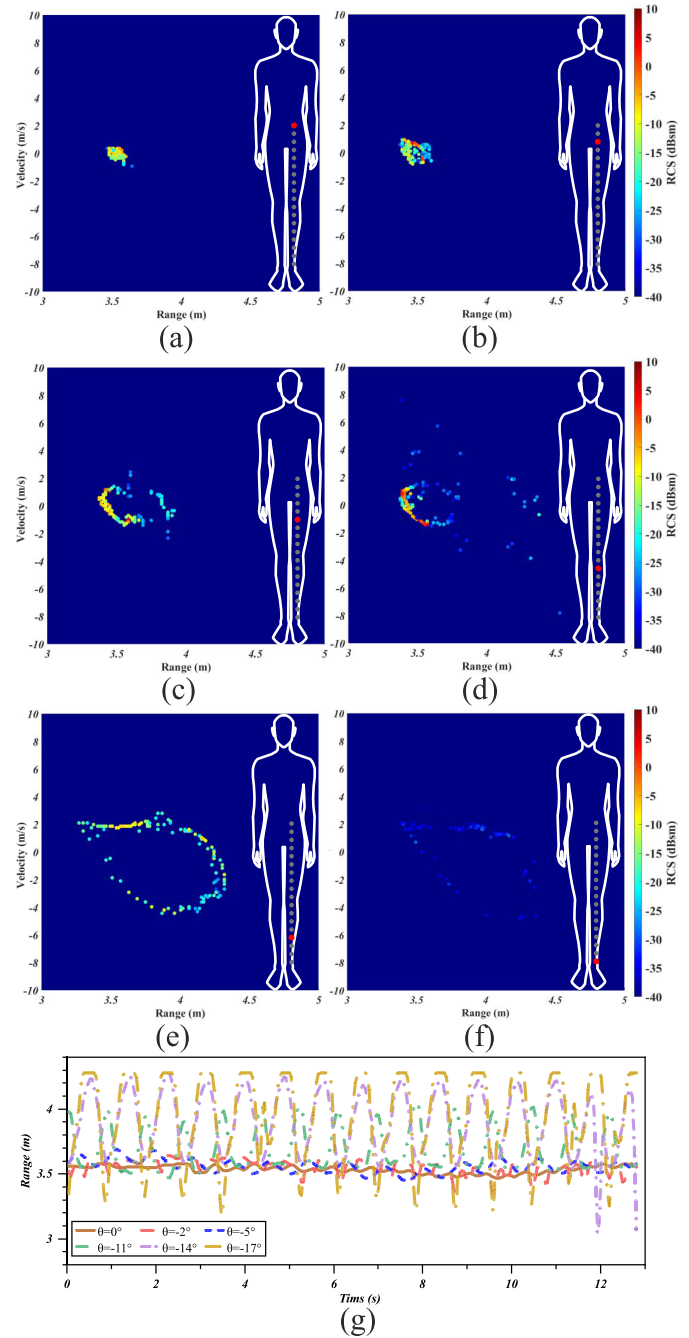


Fig. 8. Extracted range, velocity, and RCS data of a jogging human with a set speed of 1.94 m/s. The measured scattering points are along the left leg ($\varphi = -1^\circ$) with elevation angles (a) $\theta = 0^\circ$, (b) $\theta = -2^\circ$, (c) $\theta = -5^\circ$, (d) $\theta = -11^\circ$, (e) $\theta = -14^\circ$, (f) $\theta = -17^\circ$, and (g) extracted range information corresponding to sub-figures (a)–(f) from the collected MoCap data.

a larger variation of the range, which can be clearly seen in Fig. 8(b)–(f). The plots also show a closed curve, which can be seen, e.g., in Fig. 8(e), where an ellipsoidal curve is measured. This is clear since the leg moves from the back to the front and again back, resulting in a smaller and larger distance to the radar and subsequently in a positive and negative velocity. As illustrated in these figures, the value of the RCS changes with the position of the body part as well as the viewing angle of the radar during the motion. Fig. 8(g) shows the range

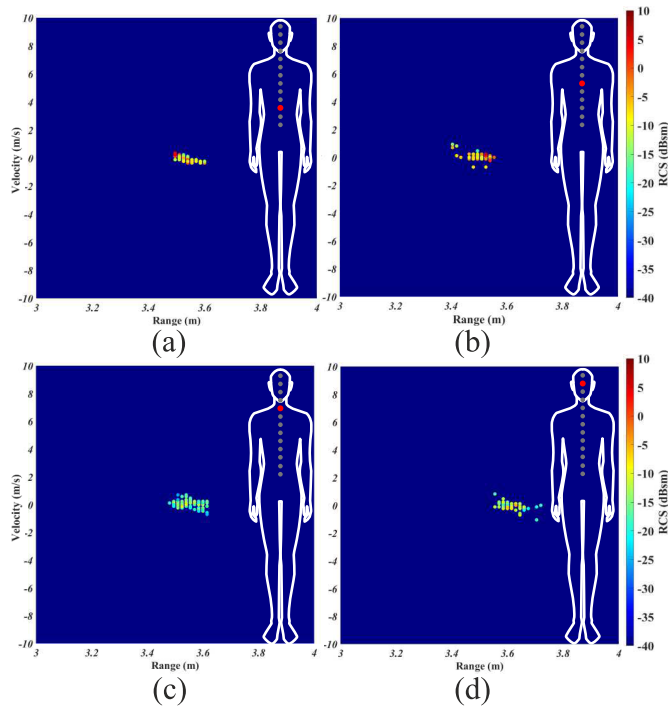


Fig. 9. Extracted range, velocity, and RCS data of a jogging human with a set speed of 1.94 m/s. The measured scattering points are along the torso-head ($\varphi = 0^\circ$) with elevation angles (a) $\theta = 3^\circ$, (b) $\theta = 6^\circ$, (c) $\theta = 9^\circ$, and (d) $\theta = 12^\circ$.

data extracted from the collected MoCap data corresponding to Fig. 8(a)–(f). These data are in good agreement with the radar range data.

Fig. 9(a)–(d) shows the extracted velocity information for the torso-head region of the jogging person at the azimuth angle of 0° . The plotted range-velocity information shows that this human body region has less dynamic behavior in comparison with the leg and hand regions. By comparing the RCS values of the detected points, it can be interpreted that the center part of the torso region has stronger backscattering behavior. As expected, the RCS values of the head region are the weakest.

The extracted radar signatures of human motion in the left-hand region are shown in Fig. 10(a)–(d). The ellipsoidal path is also in the extracted range-velocity plots of this region in the different elevation angles. The velocity of the extracted scattering points is decreasing with increasing elevation angles and approaching the shoulder area of the test person.

For quantitative comparison between the time-varying RCS values from the human extremities, the measured RCS values of similar body regions in two different situations: i.e., static and jogging, are inspected in Fig. 11. The calculated RCS values are related to the left leg, in the radar scanning area of $\theta = -5^\circ$ and $\varphi = -1^\circ$, and torso, in the radar scanning area of $\theta = 6^\circ$ and $\varphi = 0^\circ$. As expected, the torso has a stronger backscattering behavior in the static situation compared to the leg. The calculated RCS values from the same body region with changing the human situation show that RCS values are changing around the RCS value of the static situation. It can be noticed that in jogging situations, the RCS values

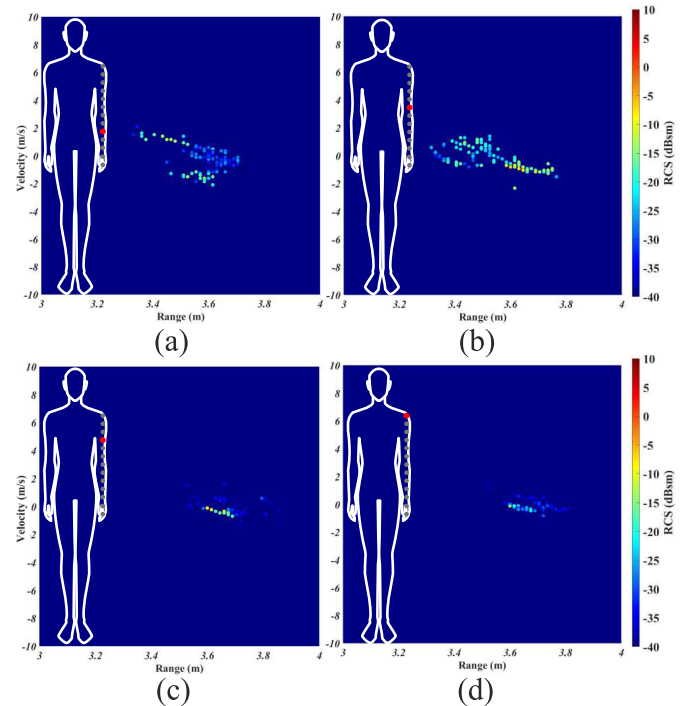


Fig. 10. Extracted range, velocity, and RCS data of a jogging human with a set speed of 1.94 m/s. The measured scattering points are along the left hand ($\varphi = -4.5^\circ$) with elevation angles (a) $\theta = 2^\circ$, (b) $\theta = 5^\circ$, (c) $\theta = 7^\circ$, and (d) $\theta = 10^\circ$.

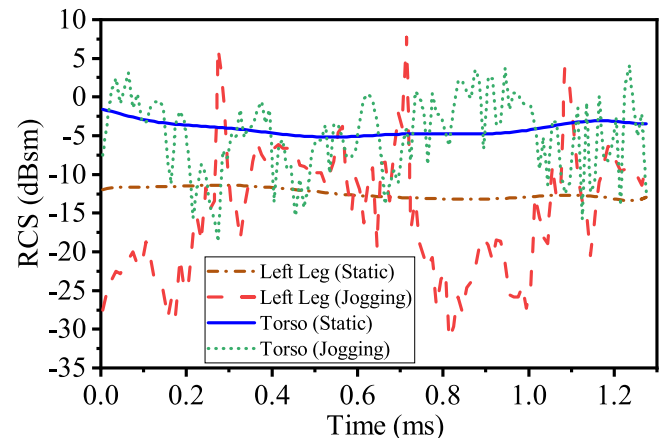


Fig. 11. Corresponding RCS values of the left leg, in the radar scanning area of $\theta = -5^\circ$ and $\varphi = -1^\circ$, and torso, in the radar scanning area of $\theta = 6^\circ$ and $\varphi = 0^\circ$, of the human body in the static and jogging situation.

vary extremely (± 18 dBsm) around the RCS values of the static human. However, the RCS variation of the torso region (± 11 dBsm) under examination when the person is jogging, is less than the leg region.

For comparing the velocity of human motion, the extracted range-velocity information of the test person from its left leg is analyzed in walking (0.69 m/s) and jogging (1.94 m/s) situations. Fig. 12(a)–(c) show the range, velocity, and RCS of the jogging human in elevation angles of $\theta = 0^\circ$, $\theta = -8^\circ$, and $\theta = -14^\circ$ and for the walking human in Fig. 12(d)–(f), respectively. The investigation of the measurement results in

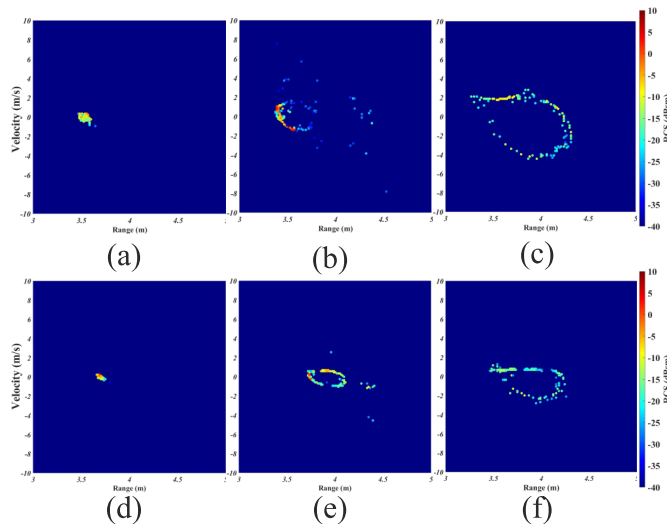


Fig. 12. Extracted range, velocity, and RCS data along the left leg ($\phi = -1^\circ$) of a human jogging (1.94 m/s) and walking (0.69 m/s) (a) jogging ($\theta = 0^\circ$), (b) jogging ($\theta = -8^\circ$), (c) jogging ($\theta = -14^\circ$), (d) walking ($\theta = 0^\circ$), (e) walking ($\theta = -8^\circ$), and (f) walking ($\theta = -14^\circ$).

Fig. 12, shows that the size of the ellipsoidal path increases with increasing the velocity of human motion.

V. CONCLUSION

In this work, a measurement setup that is capable of capturing the radar data of a human in motion in combination with the MoCap technique is introduced. This setup can simultaneously capture human motion by numerous cameras from different viewing angles. Using MoCap, it is possible to extract a highly realistic model of a human body in motion that can be used for simulations. However, the focus of this article is set to collect radar information of the body in motion that can later be combined with the MoCap model. From the radar data the range, velocity, and RCS value of distinctive body regions can be extracted. The EFE technique is utilized to calculate the range and velocity information from the measured raw data. The technique is validated by using a very accurate linear motor on which a corner reflector is moved with a constant speed and a constant deceleration, respectively. Both values have been calculated by the measured radar data and show an excellent agreement with the data of the linear stage, thus validating the concept and the calculation procedure.

The procedure was further enhanced to measure the movement of body parts of a human in walking and jogging situations. The scanning of the body region was performed by rotating a high directive radar antenna in 1° steps in both azimuth and elevation directions, covering the complete body region of interest. Additionally, the large bandwidth of the radar systems allows for a high radial resolution of the measured area. The calibration procedure of the empty room and the normalization of the RCS data were explained in detail. Several measurements have been performed in selected body regions, i.e., torso-head, hands, and legs. The range, velocity, and RCS plots of the different body regions have been shown and analyzed. It can be seen that depending on the positions

on the surface of the body; the measured points can be clearly distinguished by range and velocity. Furthermore, the RCS values of the body parts do not only depend on their position along the body but also on their viewing angle by the radar during the movement. Thus, this data can be used to develop highly realistic models for human motion in traffic scenarios combining very realistic dynamics and also very accurate radar models, including the micro-Doppler effects as well as the corresponding RCS values. Furthermore, the extracted radar data of the person enables activity recognition.

To the best of the authors' knowledge, it is the first time that a radar model can be developed, including both RCS and velocity of body parts, to form a comprehensive model that can now even be combined with a realistic motion model. Furthermore, the MoCap model can be assigned to different colored or textured clothing, also enabling a combined camera-radar model, which is, however, not the focus of this article. These enhanced models can later be used for simulation of the radar wave propagation, which is necessary either for software-in-the-loop (SiL), hardware-in-the-loop (HiL), or vehicle-in-the-loop (ViL) testing of advanced driver assistance system (ADAS) components.

ACKNOWLEDGMENT

The authors acknowledge H. Ott as the human under test during the measurement and M. Hennrich from HHVISION, Cologne, Germany, for providing the test environment.

REFERENCES

- [1] J. Park et al., "Simulation and analysis of polarimetric radar signatures of human gaits," *IEEE Trans. Aerosp. Electron. Syst.*, vol. 50, no. 3, pp. 2164–2175, Jul. 2014.
- [2] S. Abadpour, S. Marahrens, M. Pauli, J. Siska, N. Pohl, and T. Zwick, "Backscattering behavior of vulnerable road users based on high-resolution RCS measurements," *IEEE Trans. Microw. Theory Techn.*, vol. 70, no. 3, pp. 1582–1593, Mar. 2022.
- [3] M. Stolz, E. Schubert, F. Meinel, M. Kunert, and W. Menzel, "Multi-target reflection point model of cyclists for automotive radar," in *Proc. Eur. Radar Conf.*, Nuremberg, Germany, Oct. 2017, pp. 94–97.
- [4] A. Angelov, A. Robertson, and R. Murraysmith, "Practical classification of different moving targets using automotive radar and deep neural networks," *IET Radar, Sonar Navigat.*, vol. 12, no. 10, pp. 1082–1089, 2018.
- [5] R. Prophet, M. Hoffmann, A. Ossowska, W. Malik, C. Sturm, and M. Vossiek, "Pedestrian classification for 79 GHz automotive radar systems," in *Proc. IEEE Intell. Vehicles Symp. (IV)*, Jun. 2018, pp. 1265–1270.
- [6] R. Du, Y. Fan, and J. Wang, "Pedestrian and bicyclist identification through micro Doppler signature with different approaching aspect angles," *IEEE Sensors J.*, vol. 18, no. 9, pp. 3827–3835, May 2018.
- [7] T. Dallmann, J.-K. Mende, and S. Wald, "ATRIUM: A radar target simulator for complex traffic scenarios," in *Proc. IEEE MTT-S Int. Conf. Microw. Intell. Mobility (ICMIM)*, Apr. 2018, pp. 1–4.
- [8] J. Park et al., "Software defined radar studies of human motion signatures," in *Proc. IEEE Radar Conf.*, May 2012, pp. 596–601.
- [9] J. Park and J. T. Johnson, "Measurements and simulations of multi-frequency human radar signatures," in *Proc. IEEE Int. Symp. Antennas Propag.*, Jul. 2012, pp. 1–2.
- [10] V. C. Chen, F. Li, S. S. Ho, and H. Wechsler, "Micro-Doppler effect in radar: Phenomenon, model, and simulation study," *IEEE Trans. Aerosp. Electron. Syst.*, vol. 42, no. 1, pp. 2–21, Mar. 2006.
- [11] V. C. Chen, "Doppler signatures of radar backscattering from objects with micro-motions," *IET Signal Process.*, vol. 2, no. 3, pp. 291–300, Sep. 2008.
- [12] R. M. Narayanan and M. Zenaldin, "Radar micro-Doppler signatures of various human activities," *IET Radar, Sonar Navigat.*, vol. 9, no. 9, pp. 1205–1215, 2015.

- [13] A. D. Singh, S. S. Ram, and S. Vishwakarma, "Simulation of the radar cross-section of dynamic human motions using virtual reality data and ray tracing," in *Proc. IEEE Radar Conf. (RadarConf18)*, Apr. 2018, pp. 1555–1560.
- [14] Y. Deep et al., "Radar cross-sections of pedestrians at automotive radar frequencies using ray tracing and point scatterer modelling," *IET Radar, Sonar Navigat.*, vol. 14, no. 6, pp. 833–844, Jun. 2020.
- [15] C. Karabacak, S. Z. Gurbuz, A. C. Gurbuz, M. B. Guldogan, G. Hendeby, and F. Gustafsson, "Knowledge exploitation for human micro-Doppler classification," *IEEE Geosci. Remote Sens. Lett.*, vol. 12, no. 10, pp. 2125–2129, Oct. 2015.
- [16] K. Ishak, N. Appenrodt, J. Dickmann, and C. Waldschmidt, "Human motion training data generation for radar based deep learning applications," in *Proc. IEEE MTT-S Int. Conf. Microw. Intell. Mobility (ICMIM)*, Apr. 2018, pp. 1–4.
- [17] B. Erol, S. Z. Gurbuz, and M. G. Amin, "GAN-based synthetic radar micro-Doppler augmentations for improved human activity recognition," in *Proc. IEEE Radar Conf. (RadarConf)*, Apr. 2019, pp. 1–5.
- [18] I. Alnujaim, D. Oh, and Y. Kim, "Generative adversarial networks to augment micro-Doppler signatures for the classification of human activity," in *Proc. IGARSS - IEEE Int. Geosci. Remote Sens. Symp.*, Jul. 2019, pp. 9459–9461.
- [19] M. Arsalan, A. Santra, and C. Will, "Improved contactless heartbeat estimation in FMCW radar via Kalman filter tracking," *IEEE Sensors Lett.*, vol. 4, no. 5, pp. 1–4, May 2020.
- [20] S. Ayhan, S. Scherr, P. Pahl, T. Kayser, M. Pauli, and T. Zwick, "High-accuracy range detection radar sensor for hydraulic cylinders," *IEEE Sensors J.*, vol. 14, no. 3, pp. 734–746, Mar. 2014.
- [21] A. Anghel, G. Vasile, R. Cacoveanu, C. Ioana, and S. Ciochina, "Short-range wideband FMCW radar for millimetric displacement measurements," *IEEE Trans. Geosci. Remote Sens.*, vol. 52, no. 9, pp. 5633–5642, Sep. 2014.
- [22] L. Piotrowsky, T. Jaeschke, S. Kueppers, J. Siska, and N. Pohl, "Enabling high accuracy distance measurements with FMCW radar sensors," *IEEE Trans. Microw. Theory Techn.*, vol. 67, no. 12, pp. 5360–5371, Dec. 2019.
- [23] L. Piotrowsky and N. Pohl, "Spatially resolved fast-time vibrometry using ultrawideband FMCW radar systems," *IEEE Trans. Microw. Theory Techn.*, vol. 69, no. 1, pp. 1082–1095, Jan. 2021.
- [24] J.-J. Lin, Y.-P. Li, W.-C. Hsu, and T.-S. Lee, "Design of an FMCW radar baseband signal processing system for automotive application," *SpringerPlus*, vol. 5, no. 1, pp. 1–16, Jan. 2016.
- [25] M. Kitagawa and B. Windsor, *MoCap for Artists: Workflow and Techniques for Motion Capture*, 1st ed. Amsterdam, The Netherlands: Elsevier, May 2008.
- [26] A. Menache, *Understanding Motion Capture for Computer Animation*, 2nd ed. Burlington, MA, USA: Morgan Kaufmann, Dec. 2011.
- [27] *Optitrack*. Accessed: May 16, 2022. [Online]. Available: <https://optitrack.com/cameras/primex-13/specs.html>
- [28] M. Chen and C.-C. Chen, "RCS patterns of pedestrians at 76–77 GHz," *IEEE Antennas Propag. Mag.*, vol. 56, no. 4, pp. 252–263, Aug. 2014.
- [29] N. Yamada, Y. Tanaka, and K. Nishikawa, "Radar cross section for pedestrian in 76GHz band," in *Proc. Eur. Microw. Conf.*, Oct. 2005, pp. 1018–10228.
- [30] E. Marchetti et al., "Radar cross-section of pedestrians in the low-THz band," *IET Radar, Sonar Navigat.*, vol. 12, no. 10, pp. 1104–1113, Sep. 2018.



Sveda Abadpour (Member, IEEE) received the B.Sc. degree in electrical engineering and information technology from the Iran University of Science and Technology (IUST), Tehran, Iran, in 2008, and the M.Sc. degree in electrical engineering and information technology from the Amirkabir University of Technology (AUT), Tehran, in 2011. She is currently pursuing the Ph.D. degree in electrical engineering at the Institute of Radio Frequency Engineering and Electronics (IHE), Karlsruhe Institute of Technology (KIT), Karlsruhe, Germany.

Her current research interests include automotive radar channel modeling and electromagnetic wave propagation. Her work focuses on RCS measurement for traffic participants and the development of radar models for the use in over-the-air (OTA) vehicle-in-the-loop (ViL) test method.



Mario Pauli (Senior Member, IEEE) received the M.S.E.E. degree in electrical engineering from the University of Karlsruhe, Karlsruhe, Germany, in 2003, and the Ph.D.E.E. degree from the Karlsruhe Institute of Technology, Karlsruhe, in 2011.

In 2002, he spent four months at the IBM T. J. Watson Research Center, Yorktown Heights, NY, USA, working on time- and frequency-domain measurement systems for the characterization of the 60 GHz indoor radio channel. From 2004 to 2011, he was a Research Assistant with the Institut für Höchstfrequenztechnik und Elektronik (IHE), University of Karlsruhe. Since 2011, he has been a Senior Researcher and a permanent Lecturer with the Institute of Radio Frequency Engineering and Electronics (IHE), Karlsruhe Institute of Technology (KIT). He has served as a Lecturer for radar and smart antennas of the Carl Cranz Series for Scientific Education. He is currently a Co-Founder and the Managing Director of PKTEC GmbH, Karlsruhe, and a Co-Founder of Wellenzahl Radar- und Sensortechnik GmbH & Company KG, Karlsruhe. His current research interests include radar and sensor systems, RCS measurements, antennas, wave propagation, and millimeter-wave packaging.



Christian Schyr received the Diploma degree in mechanical engineering from the Vienna University of Technology, Vienna, Austria, in 1992, the M.Sc. degree in aerospace engineering from The University of Texas at Austin, Austin, TX, USA, in 1994, and the Ph.D. degree from the Karlsruhe Institute of Technology, Karlsruhe, Germany, in 2006.

He is currently a Principal Engineer with the Advanced Solution Laboratory, AVL Deutschland GmbH, Karlsruhe. His main research interests are new development methods and tools for highly automated and electrified mobility systems in the automotive, agricultural, and maritime domains. He has authored more than 100 scientific publications and is also the inventor of eight patents. His professional experience involved positions in software development, product management, and working on numerous research projects in national and European-funded programs and research clusters.

Dr. Schyr has served on the Steering Board of the ARTEMIS Industrial Association and is currently on the Steering Board of the VVMethods Project.



Florian Klein received the master's degree in automotive engineering from the Cologne University of Applied Sciences, Cologne, Germany, in 2018.

In 2019, he was appointed as the Head of research and development projects in the field of VR applications at HHVISION, Cologne. In addition to gaining economic developments and new research projects, he currently works on the integration of new methods and working methods in the field of VR. His core task is the investigation between architecture and automotive engineering in virtual reality.



Rene Degen received the M.Sc. degree in mechatronics from the Cologne University of Applied Sciences, Cologne, Germany, in 2018. He is currently pursuing the cooperative Ph.D. degree at Uppsala University, Uppsala, Sweden, and the Cologne University of Applied Sciences, where he focuses on the development of a virtual test environment for highly automated vehicle systems.

Since 2017, he has been working as a Research Associate with the CAD CAM Center, Cologne, where his research activities were mainly in the field of robotics, mechatronics, and future mobility systems. In 2020, he became the Chief Engineer of the CAD CAM Center in the field of mechatronics.



Jan Siska (Member, IEEE) received the B.Sc. and M.Sc. degrees in electrical and information engineering from Ruhr University Bochum, Bochum, Germany, in 2015 and 2018, respectively, where he is currently pursuing the Ph.D. degree at the Institute of Integrated Systems.

His main research interests include digital signal processing, millimeter-wave radar system design, and vital sign detection using frequency-modulated continuous-wave (FMCW) radar sensors.

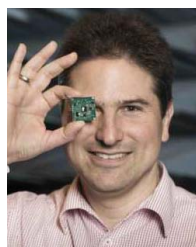


Nils Pohl (Senior Member, IEEE) received the Dipl.Ing. and Dr.Ing. degrees in electrical engineering from Ruhr University Bochum, Bochum, Germany, in 2005 and 2010, respectively.

From 2006 to 2011, he was a Research Assistant with Ruhr University Bochum, where he was involved in integrated circuits for millimeter-wave (mm-wave) radar applications. In 2011, he became an Assistant Professor with Ruhr University Bochum. In 2013, he became the Head of the Department of mm-wave Radar and High Frequency

Sensors, Fraunhofer FHR, Wachtberg, Germany. In 2016, he became a Full Professor for integrated systems with Ruhr University Bochum. In parallel, he is also the head of the Research Group for Integrated Radar Sensors, Fraunhofer FHR. He has authored or coauthored more than 200 scientific articles and has issued several patents. His current research interests include ultrawideband mm-wave radar, design, and optimization of mm-wave integrated SiGe circuits and system concepts with frequencies up to 300 GHz and above, as well as frequency synthesis and antennas.

Prof. Pohl was a co-recipient of the 2009 EEEfCom Innovation Award, the Best Paper Award at European Microwave Integrated Circuit (EUMIC) 2012, the Best Demo Award at Radio and Wireless Week (RWW) 2015, and the Best Student Paper Awards at RadarConf 2020 and RWW 2021. He was a recipient of the Karl-Arnold Award of the North Rhine-Westphalian Academy of Sciences, Humanities and the Arts in 2013, and the IEEE Microwave Theory and Technique (MTT) Outstanding Young Engineer Award in 2018.



Thomas Zwick (Fellow, IEEE) received the M.S.E.E. and Ph.D.E.E. degrees from Universität Karlsruhe (TH), Karlsruhe, Germany, in 1994 and 1999, respectively.

From 1994 to 2001, he was a Research Assistant with the Institut für Höchstfrequenztechnik und Elektronik (IHE), Universität Karlsruhe (TH). In February 2001, he joined the IBM T. J. Watson Research Center, IBM, Yorktown Heights, NY, USA, as a Research Staff Member. From October 2004 to September 2007, he was with Siemens AG, Lindau,

Germany. During this period, he managed the RF Development Team for automotive radars. In October 2007, he became a Full Professor with the Karlsruhe Institute of Technology (KIT), Karlsruhe. He is currently the Director of the Institute of Radio Frequency Engineering and Electronics (IHE), KIT. He is a coeditor of three books, the author or a coauthor of 120 journal articles, more than 400 contributions at international conferences, and 15 granted patents. His research topics include wave propagation, stochastic channel modeling, channel measurement techniques, material measurements, microwave techniques, millimeter-wave antenna design, wireless communication, and radar system design.

Dr. Zwick has been a member of the Heidelberg Academy of Sciences and Humanities since 2017 and acatech (German National Academy of Science and Engineering) since 2019. His research team has received more than ten best paper awards at international conferences. He has served on the Technical Program Committee (TPC) for several scientific conferences. He was the General Chair of the International Workshop on Antenna Technology (iWAT 2013), Karlsruhe, in 2013, and the IEEE Microwave Theory and Technique (MTT)-S International Conference on Microwaves for Intelligent Mobility (ICMIM), Heidelberg, in 2015. He was also the TPC Chair of the European Microwave Conference (EuMC) in 2013 and the General TPC Chair of the European Microwave Week (EuMW) in 2017. In 2023, he will be the General Chair of EuMW, Berlin. From 2008 to 2015, he was the President of the Institute for Microwaves and Antennas (IMA). He became selected as a Distinguished IEEE Microwave Lecturer for the 2013–2015 period with his lecture on “QFN based packaging concepts for millimeter-wave transceivers.” In 2019, he became the Editor-in-Chief of the IEEE MICROWAVE AND WIRELESS COMPONENTS LETTERS.